Journal of Catalysis 419 (2023) 1–8

Contents lists available at ScienceDirect

Journal of Catalysis

journal homepage: www.elsevier.com/locate/jcat

Overcoming energy mismatch of metal oxide semiconductor catalysts for CO_2 reduction with triboelectric plasma

Bao Zhang [a,1], Qinglong Ru [a,1], Liangliang Liu [a,1], Jiao Wang [a], Youning Zhang [a], Ke Zhao [a], Guangqin Gu [a], Xiaochen Xiang [a], Sumin Li [a], Yifei Zhu [b], Yu Jia [a], Gang Cheng [a,*], Zuliang Du [a,*]

[a] *Key Lab for Special Functional Materials, Ministry of Education, National & Local Joint Engineering Research Center for High-efficiency Display and Lighting Technology, School of Materials Science and Engineering, and Collaborative Innovation Center of Nano Functional Materials and Applications, Henan University, Kaifeng 475004, China*
[b] *Institute of Aero-engine, School of Mechanical Engineering, Xi'an Jiaotong University, Xi'an 710049, China*

ARTICLE INFO

Article history:
Received 27 October 2022
Revised 17 January 2023
Accepted 24 January 2023
Available online 27 January 2023

Keywords:
Triboelectric plasma
Metal oxide semiconductor
Energy mismatch
CO_2^- reactive species
Surface lattice oxygen activation

ABSTRACT

The activities of semiconductor-based catalytic reactions are limited by mismatch between energy bandgaps of semiconductors and redox potentials of inert small molecules, especially for stable molecules, such as CO_2. Herein, a triboelectric plasma catalytic system using metal oxide catalysts has been developed, which reduces CO_2 to CO at room temperature and atmospheric pressure. Among the various metal oxide semiconductors, TiO_2 catalyst exhibited the best activity, reaching a production rate of $0.14 \text{mmol}\cdot g_{cat}^{-1}\cdot h^{-1}$, and an energy efficiency of 5.3 % for the conversion of electrical to chemical energy. In triboelectric plasma, CO_2 molecules were pre-activated to form the transient CO_2^- anions, and the limiting step of electron transfer between TiO_2 and CO_2 was avoided, overcoming the energy mismatch between catalyst and CO_2. The energy barrier of CO_2 dissociation was markedly reduced to 0.18 eV. This work provides an effective strategy to overcome the energy bandgap restriction inherent in semiconductor-based catalytic reactions.

1. Introduction

In a catalytic reaction, substrate activation is the key step, and this step is closely related to the activity of the catalyst [1,2]. More specifically, substrate activation is determined by the energy band structure and surface active sites of the catalyst [1]. One of the main pathways involved in substrate activation is substrate ionization, such as the single electron reduction of CO_2 molecules and activation of CO_2 to CO_2^- anions during the reduction of CO_2 to CO [3,4]. During such an ionization process, the substrates are generally in the low-energy state, while the highly reactive ions are in the high-energy state, thereby driving the chemical reactions characterized by the movement of electrons or holes [5]. In a semiconductor-based catalytic reaction, substrate ionization is realized through the charge-transfer process between the semiconductor and substrate [6,7]. In such a system, the energy band structure and active sites are adjusted by doping or through the construction of heterojunctions to match the oxidation–reduction potential of the substrate ionization process [1,8–14]. Using light as an excitation source, photogenerated electrons and holes can further facilitate the charge transfer process between the semiconductor and the substrate, thereby accelerating substrate ionization and the surface redox reaction (see Fig. 1a) [8,10,11,15]. However, a mismatch between the energy bandgaps of semiconductors and the energy levels of inert small molecules, such as CO_2 and N_2, hinders the transfer of charge from the semiconductors to these small molecules, resulting in low catalytic activities and energy conversion efficiencies [8,9,11,16]. Taking the TiO_2-based photocatalytic reduction of CO_2 as a theoretical example, the lowest unoccupied molecular orbital (LUMO) level of CO_2 is 1.4 eV higher than the conduction band minimum (CBM) of the TiO_2 photocatalyst (Fig. 1b) [8,9]. Moreover, the CO_2 LUMO level is significantly higher than those of the conduction bands of almost all semiconductors; hence, the electrons present in the conduction bands of the semiconductors cannot migrate to the CO_2 molecule [8,9]. The development of an efficient semiconductor-based catalytic system is therefore necessary to overcome the inherent limitations of semiconductor energy bandgaps in catalytic reactions.

An effective means to overcome these limitations is the use of external stimuli to assist substrate activation [17–19] and to construct a new semiconductor-based catalytic system. In this context, triboelectric plasma, which is generated via gas ionization [20–24]

---

* Corresponding authors.

E-mail addresses: chenggang@henu.edu.cn (G. Cheng), zld@henu.edu.cn (Z. Du).

[1] These authors contributed equally to this work: Bao Zhang, Qinglong Ru, Liangliang Liu.

https://doi.org/10.1016/j.jcat.2023.01.031
0021-9517/

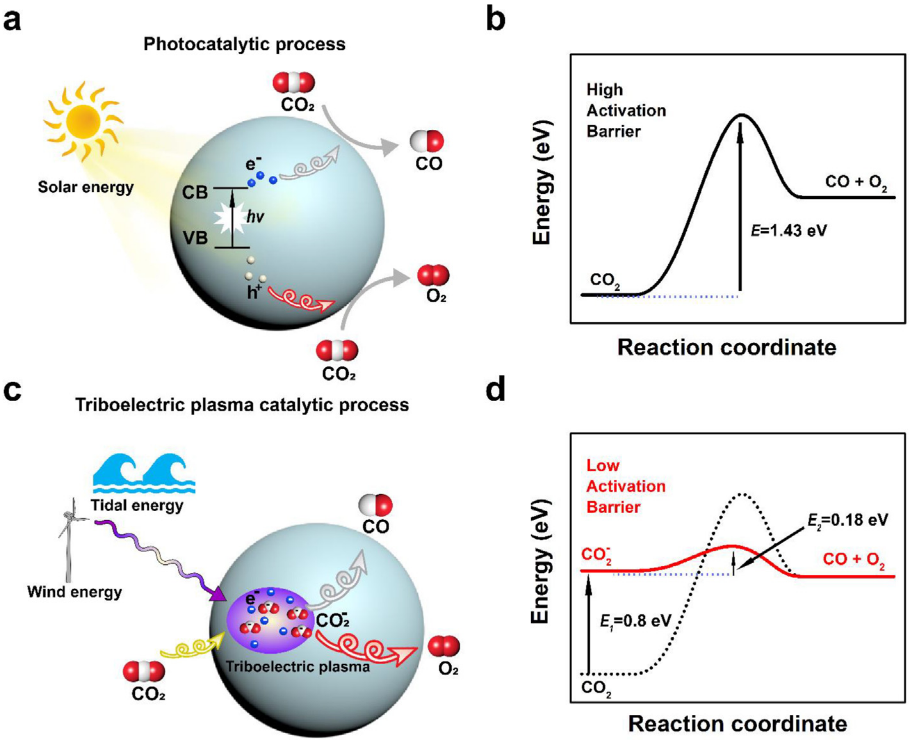

Fig. 1. Comparison of photocatalytic and triboelectric plasma-catalyzed process on semiconductors. (a) Photocatalytic process on a semiconductor. (b) Schematic representation of the potential energy surface for the reduction of CO_2 via the photocatalytic process. (c) Triboelectric plasma catalytic process on a semiconductor. (d) Schematic representation of the potential energy surface for the reduction of CO_2 via the triboelectric plasma catalytic process.

and is driven by a triboelectric nanogenerator, could directly transfer the charge to the substrate molecules [25,26]. This step can be referred to as pre-activation of the substrate [27,28]. For example, electrons are injected into the LUMO level of CO_2 to form CO_2^- anions, realizing the pre-activation of CO_2 [20]. During the gas ionization process, the temperature of the gas molecules remains relatively constant, and reactive species, such as CO_2^- anions, are in the high-energy state, thereby allowing chemical conversion of the substrates under mild conditions [21,22]. Moreover, triboelectric plasma can be powered by dispersed, abundant, and renewable mechanical energy from the surrounding environment [29–36], which is conducive to small-scale CO_2 fixation (Fig. 1c). Similar to the photocatalytic reaction system, the triboelectric plasma catalytic system can be constructed by introducing a semiconductor catalyst into the triboelectric plasma. In this system, the gas ionization process that leads to the generation of highly reactive ions in the triboelectric plasma replaces the charge-transfer process from the semiconductor to the inert molecules, and it can effectively overcome the limitations of the energy mismatch between these two species; importantly, semiconductor catalysts contain a large number of surface-active sites, which can stabilize the highly reactive gas ions (Fig. 1d). The triboelectric plasma catalytic system is therefore expected to address the limitations of the energy band structure and provide additional surface-active sites to improve the overall energy efficiency and catalytic activity.

Thus, we report the construction of a catalytic system using a combination of triboelectric plasma and a metal oxide semiconductor. This catalytic system is used for the reduction of CO_2 at room temperature (25 °C) and atmospheric pressure, and the catalytic activity and energy conversion efficiency are determined. In addition, electron paramagnetic resonance (EPR) spectroscopy and Fourier transform infrared (FT-IR) spectroscopy are used to determine the species that are present during the reaction, while X-ray photoelectron spectroscopy (XPS), EPR spectroscopy, and Raman spectroscopy are used to probe the formation of oxygen vacancies. Finally, a mechanism for this catalytic process is proposed.

2. Experimental details

2.1. Construction of triboelectric nanogenerator (TENG)

A triboelectric nanogenerator (TENG) was operated by an electric motor and was used to drive the triboelectric plasma catalytic CO_2 reduction system. More specifically, a freestanding-rotating TENG with a radius of 10 cm was selected as the model system for this study. The TENG was composed of two parts, namely a static metal layer and a freestanding rotational triboelectric layer, which occupied 1/2 and 1/4 of the area of the circular nanogenerator, respectively. A polytetrafluoroethylene (PTFE) film (5 μm) was used as the rotating triboelectric layer, and a printed circuit board with a Cu film (60 μm) was used as both the other triboelectric layer and the electrode. Both films were attached to circular polymethyl methacrylate (PMMA) substrates. The four sections of the metal layers were alternately linked, and the two separated sectors were connected by inner or outer metallic Cu to form two TENG electrodes.

2.2. Triboelectric plasma catalytic CO_2 reduction powered by mechanical energy

The mechanically-driven triboelectric plasma catalytic CO_2 reduction process was performed in a custom-made 500 mL glass device at room temperature (25 °C) and atmospheric pressure. The glass reactor was purged thrice with high-purity CO_2 (99.999 %, Kaifeng Shengyuan Gas Co., Ltd., China) prior to use. A needle–plate configuration gas discharge system was used in the glass reactor, where a W needle (curvature radius of 5 μm) was used as the counter electrode. The metal oxides on the Pt plate functioned as the working electrode. The two discharge electrodes were perpendicular to one another and were linked to the TENG electrodes with Cu wires. The distance (d) between the working electrode and the W needle was regulated using a three-dimensional (3D) micromanipulation stage. The triboelectric plasma was operated at a negative polarity, where the W needle was connected to the negative polarity of the rectifier bridge, and the working electrode was connected to the positive polarity of the rectifier bridge.

The working electrode was prepared as follows: The TiO_2 catalyst (P25) was obtained from Degussa. Au, Pt, SiO_2, CuO, ZnO, CeO_2, anatase phase TiO_2, and rutile phase TiO_2 were purchased from Sigma-Aldrich, China. A Pt plate was used to connect the positive polarity of the rectifier bridge through Cu wires, and it was also used as a substrate for loading the semiconductor catalysts (i.e. SiO_2, CuO, ZnO, CeO_2, anatase phase TiO_2, and rutile phase TiO_2). The Pt plane was sonicated in ethanol (99.97 %, Tianjin Fuyu Chemical, China) and deionized water three times. Then, it was dried at 60 °C in an oven. The semiconductor catalysts were loaded onto the Pt plate using the spin coating technique. Taking TiO_2 as an example, after suspending the TiO_2 sample powder in deionized water with continuous stirring, the resulting slurry was evenly spread onto the Pt plate and dried at room temperature (25 °C) under atmospheric conditions. The area of the working electrode was 1 cm^2.

2.3. Energy efficiency during conversion of electrical to chemical energy ($\eta_{ele-chem}$)

The discharge current and voltage were measured using a two-channel electrometer (Keithley 6514, Tektronix, USA), wherein one channel recorded the discharge current, and the other measured the discharge voltage. The discharge voltage was obtained by measuring the current when an appropriate sampling resistor (~GΩ) was introduced into the circuit. The electrical signal was measured using an acquisition card. The average electrical energy (E_{ele}) consumed by the triboelectric plasma per second was calculated as follows (Equation (1)):

$$E_{ele} = \int_0^t V \cdot I \cdot dt \tag{1}$$

where V is the discharge voltage (V), I is the discharge current (A), and t is discharge time (s).

The qualitative and quantitative analyses of the CO product were performed using gas chromatography or a gas sensitivity detector. The concentration of the CO product was calculated by using a calibration gas standard (the concentration of CO was ~ 50 ppm). The gas chromatograph was equipped with a Shincarbon column (column temperature, 90 °C), a thermal conductivity detector (TCD), and a mechanized flame ionization detector. He was used as the carrier gas.

The energy efficiency (η) during the conversion of electrical to chemical energy was calculated as follows (Equation (2)):

$$\eta_{ele-chem} = \frac{r_{CO} \cdot t \cdot \Delta_r H^{\Theta}(CO)}{E_{ele} \cdot 3600} \tag{2}$$

where r_{CO} is the evolution rate of CO ($\mu mol \cdot h^{-1}$), $\Delta_r H^{\Theta}(CO)$ is the enthalpy change for the dissociation of CO_2 (kJ/mol), and E_{ele} is the average electrical energy consumed by the triboelectric plasma (J/s).

2.4. Controlled experiments and recycling experiments

For comparison, the photocatalytic reduction of CO_2 on the TiO_2 catalyst was performed under the same conditions as those used for the triboelectric plasma catalytic CO_2 reduction reaction, i.e., under ultra violet (UV light) with a Thorlabs instrument at room temperature (25 °C) and atmospheric pressure. In addition, the thermal catalytic oxidation of CO on the TiO_2 catalyst was performed under the same conditions as those employed for the triboelectric plasma catalytic CO_2 reduction reaction.

For the isotope tracer experiments, $^{13}CO_2$ and $C^{18}O_2$ were used as the substrates under the same conditions as those used for the triboelectric plasma CO_2 reduction reaction. $^{13}CO_2$ and $C^{18}O_2$ were purchased from Wuhan New Radar Special Gas Co., Ltd. (China). The isotopic enrichments of $^{13}CO_2$ and $C^{18}O_2$ were 99 and 96 %, respectively. The isotopic analyses of the CO and O_2 products were performed at Wuhan New Radar Special Gas Co., Ltd. (China).

For the recycling experiments, the triboelectric plasma catalytic CO_2 reduction reaction was performed as described earlier; after one run, the gas in the reactor was replaced with fresh CO_2 prior to commencing the subsequent cycle.

2.5. Demonstration in natural environment

Wind was used as a direct driving force for the triboelectric plasma catalytic reduction of CO_2, to demonstrate that the triboelectric plasma catalytic system can effectively utilize the random mechanical energy provided in a natural environment. The inner diameter of the glass reaction bottle was 7 cm, the height was 13.5 cm, the reaction temperature was 20 °C, and the pressure was 1 atm. At a wind speed of approximately 3.0 m s^{-1}, the CO sensor indicator displayed a continuous increase in the CO concentration over time. After 1.5 h, the CO sensor in the reactor showed a reading of 12 ppm, which correlated to a production rate of 25.5 $\mu mol \cdot g_{cat}^{-1} \cdot h^{-1}$.

2.6. Electron paramagnetic resonance (EPR) experiments

The EPR experiments were performed at 16–18 °C using a Bruker EPR A200 X-band spectrometer (Bruker, Germany). 5,5-Dimethyl-1-pyrroline-*N*-oxide (DMPO, Sigma-Aldrich) was used as a spin-trapping reagent to capture the reactive species that were generated during the triboelectric plasma catalytic CO_2 reduction reaction. The 0.45 M aqueous DMPO solution was stored at 0 °C in the dark until it was required; the solution was degassed over three freeze–thaw cycles, and the reaction bottle was purged with CO_2 gas. The triboelectric plasma CO_2 reduction process was performed in the aqueous DMPO solution; the TiO_2/Pt electrode was immersed in the DMPO solution, and the W needle was placed above the DMPO solution. Following triboelectric plasma treatment, an aliquot (~100 μL) of the DMPO solution was removed by means of a capillary tube and was transferred to a quartz nuclear magnetic resonance (NMR) tube. The NMR tube was placed in the EPR instrument for the analysis of the sample.

2.7. Characterization of TiO_2 catalyst

The crystal structures of the samples were determined by powder X-ray diffraction measurement (XRD, Bruker D8 Advance) with Cu-Kα (0.154 nm) radiation over a scan range of 10–80°. The FT-IR difference spectra of the samples were recorded on an FT-IR/FIR spectrometer (Perkin-Elmer). The morphologies of the samples were examined using transmission electron microscopy (Tecnai G^2 Spirit, FEI), and the Raman spectra were recorded using a Renishaw (InVia Raman Microscope) spectrometer under ambient conditions (25 °C and 1 atm) with a 532 nm laser as the excitation source. The photoluminescence (PL) spectra of the samples were measured on an Edinburgh FLS1000 spectrometer under excitation by ultraviolet light with an excitation wavelength of 300 nm.

2.8. Density functional theory calculations and triboelectric plasma simulation

First-principles calculations based on the density functional theory (DFT) approach were used to study the reduction of CO_2 on an anatase (1 0 1) TiO_2 surface. The calculations were performed using the Vienna ab initio simulation package with the projector-augmented wave method [37–39]. For the exchange–correlation energy, we used the Perdew–Burke–Ernzerhof (PBE) generalized-gradient approximation functional [40]. The vacuum layer on the anatase (0 0 1) surface was 20 Å, which was sufficiently large to avoid interactions between neighboring cells. A plane wave basis was utilized with a kinetic energy cutoff of 500 eV, and k-space integration was performed with 5 × 5 × 1 meshes in the Brillouin zones of the surface slab. All atoms were allowed to relax along with the calculated forces until all the residual force components were < 0.01 eV/Å. In our calculations, the van der Waals interactions were considered using the PBE-D_3 scheme [41] to study the adsorption of CO_2 molecules. The adsorption energy of the CO_2 molecules was defined as follows (Equation (3)):

$$E_{ad} = E_{surf+CO_2} - E_{surf} - E_{CO_2} \tag{3}$$

where $E_{surf+CO_2}$ is the total energy of the surface and adsorbed CO_2, E_{surf} is the energy of the surface slab, and E_{CO_2} is the energy of a free CO_2 molecule.

The climbing image nudged elastic band (CI-NEB) method [42] was used to search for the minimal energy diffusion paths and the saddle points of the dissociation of the CO_2 molecule on an anatase (1 0 1) TiO_2 surface. Between the initial and final configurations, five images were used for the purpose of the CI-NEB calculations. Vibrational frequency calculations were performed to analyze the transition-state configurations.

The average electron energy versus time evolution was calculated using the calculation method previously reported in the literature after changing some parameter values [19,20].

3. Results and discussion

3.1. Triboelectric plasma catalytic CO_2 reduction driven by mechanical energy

A schematic diagram of the mechanically-driven triboelectric plasma catalytic CO_2 reduction set-up is illustrated in Fig. 2a, wherein the TENG, rectifier bridge, and triboelectric plasma reactor can be seen. Although a TENG can convert mechanical motion into high-voltage electrical energy to power the triboelectric plasma, we used a triboelectric generator with a low energy output to observe the interactions between the triboelectric plasma and the semiconductors [20–22]. The triboelectric plasma device contained two electrodes, namely, a W needle and a working electrode. The working electrode was stacked with a catalyst and a conductive substrate (such as a Pt plate), and when a polytetrafluoroethylene (PTFE) film was contacted with a Cu film, negative/positive triboelectric charges were generated on the surface of the PTFE/Cu film owing to the different chemical potentials. When the PTFE was rotated about its centerline axis, a potential difference of 2.5 kV was generated between the two TENG electrodes (Fig. S1). As the output voltage of the TENG exceeded the threshold voltage (~1000 V) of CO_2 gas, triboelectric plasma was generated. As shown in Fig. 2b, at the edge of the triboelectric plasma, the low energy electrons were unable to ionize the electronegative CO_2 molecules, and they were trapped with CO_2 molecules, thereby forming CO_2^- anions owing to the low energy barrier associated with this process (i.e., 0.8 eV, Equation (4)) [3,43]. When the needle–plate distance was set at 0.15 mm and the rotational speed of the TENG was 300 rpm, the ionization process of the triboelectric plasma, which is shown as a curve in Fig. 2c, was generated under a negative polarity. Over half a cycle, three unidirectional pulse voltage peaks of ~ 1.2 kV were generated, and these were accompanied by three current peaks of ~ 60 μA, thereby confirming the generation of triboelectric plasma.

$$CO_2 + e^- \rightarrow CO_2^-, \Delta H = -0.8eV \tag{4}$$

The reduction of CO_2 over different catalysts was performed along with controlled experiments at room temperature (25 °C) and atmospheric pressure for 1 h (Fig. 2d and Fig. S2–3). Under triboelectric plasma conditions (Fig. 2c), all the metal oxides supported on the Pt electrode exhibited a good CO_2 reduction performance; the TiO_2 catalyst exhibited the best catalytic activity. These results indicate that metal oxides generally exhibit CO_2 reduction properties under triboelectric plasma conditions. Furthermore, the three different crystalline phases of the TiO_2 catalysts displayed good catalytic activities, with P25 exhibiting the highest conversion of 0.14 $\text{mmol}\cdot g_{cat}^{-1}\cdot h^{-1}$, in addition to a 5.3 % energy efficiency for the conversion of electrical to chemical energy. The ^{13}C-isotope labeling experiments demonstrated that the CO originated from the CO_2 reduction reaction rather than from any contamination of the air or catalyst (Fig. S4). Hence, we selected P25 as a model catalyst to investigate the relationship between the triboelectric plasma and the semiconductors.

To further confirm the role of the triboelectric plasma, its supply was cut off from the reaction system, and the reduction of CO_2 was performed on the TiO_2 catalyst under different controlled conditions. More specifically, at room temperature (25 °C) or under ultraviolet light irradiation with a light intensity of 45 mW cm^{-2} (i.e., ~450 times the indoor light intensity), no CO was produced, thereby implying that the triboelectric plasma is the direct driving force for the reduction of CO_2 over metal oxides. According to the literature, plasma can only reduce CO_2 to CO via a direct plasma reduction process [12,19,20]. Thus, to determine the degree to which direct plasma reduction occurred in our system, Pt and Au were used to replace the metal oxide catalyst; however, their activities were close to zero. These experiments implied that metal oxides play an important role in promoting the triboelectric plasma CO_2 reduction reaction, which differs from literature reports indicating that different materials show minor influences on the CO_2 reduction activity [19,20]. These contradictory results may be attributed to the discharge characteristics of triboelectric plasma, which are closely related to the quantity of electrical energy input into the system; these input energy values differ from those presented in the literature for the direct triboelectric plasma CO_2 reduction process [7,20].

To verify the practicality of the mechanically-driven triboelectric plasma TiO_2 catalytic system, a test was performed on the roof of a building. More specifically, Video S1 shows that the triboelectric plasma TiO_2 catalytic system driven by the TENG was able to directly use the irregular wind energy collected from the environment to reduce CO_2 molecules to CO. Importantly, for this application example, an activity of 25.5 $\mu\text{mol}\cdot g_{cat}^{-1}\cdot h^{-1}$ was achieved.

3.2. Detection of reactive species involved in CO_2 reduction process

Using DMPO as the trapping agent, EPR spin-trapping technology was used to determine the CO_2-derived reactive species generated in the triboelectric plasma (Fig. 3a and Fig. S5). More specifically, in the absence of plasma, no EPR signal is generated (I), whereas under the triboelectric plasma conditions, a significant

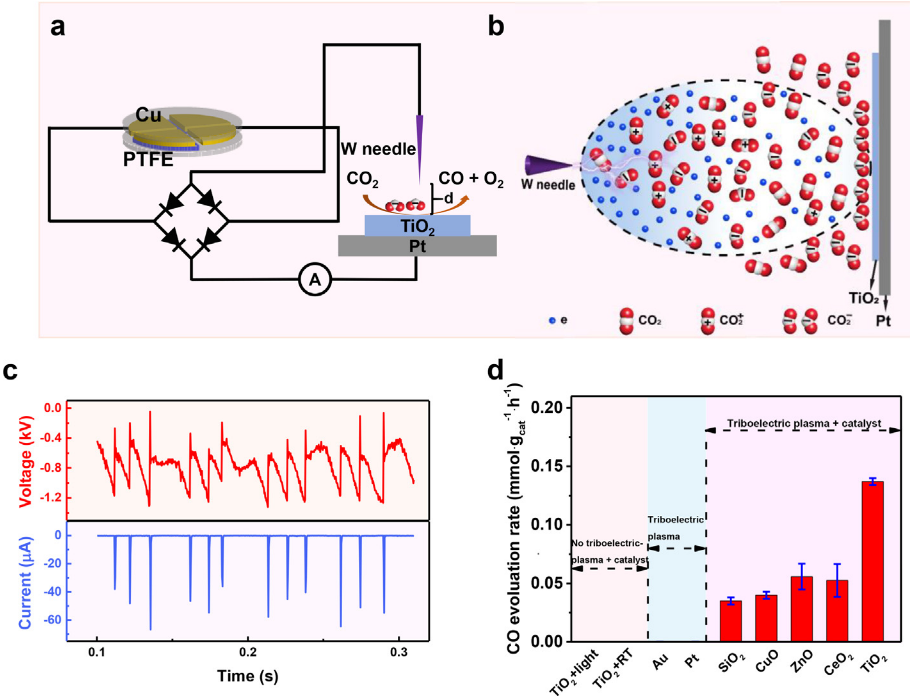

Fig. 2. Reduction of CO_2 by the triboelectric plasma system driven by mechanical energy. (a) The triboelectric plasma–metal oxide catalytic system driven by a triboelectric nanogenerator (TENG). (b) Formation of the triboelectric plasma. (c) Discharge voltage and current achieved in the triboelectric plasma. (d) CO_2 reduction under various conditions. Reaction conditions: Needle–plate distance = 0.15 mm, TENG rotational speed = 300 rpm, polarity = negative, temperature = 25 °C, pressure = atmospheric pressure, reaction time = 1 h.

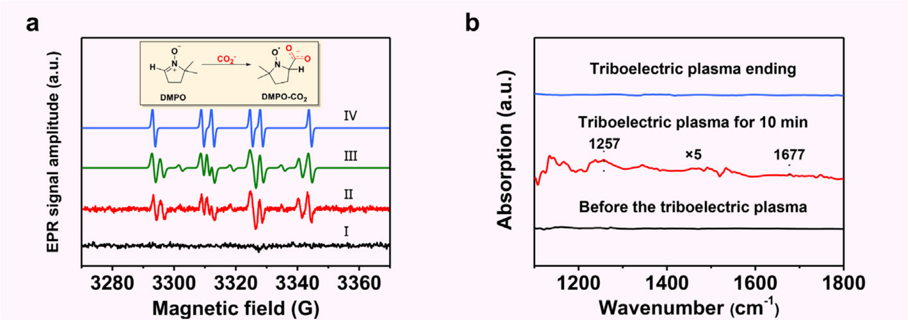

Fig. 3. CO_2-derived reactive species generated under the triboelectric plasma conditions. (a) Electron paramagnetic resonance (EPR) spectra of the reactive species during the triboelectric plasma process. (I) EPR spectrum before treatment with triboelectric plasma, (II) EPR spectrum under the triboelectric plasma conditions, (III) the simulated sum EPR spectrum, and (IV) the simulated EPR spectrum of the DMPO-CO_2^- anion. Reaction conditions: Needle–plate distance = 0.15 mm, TENG rotational speed = 300 rpm, polarity = negative, temperature = 25 °C, pressure = atmospheric pressure, reaction time = 5 min. (b) Fourier transform infrared (FT-IR) difference spectra for interaction of CO_2 with the TiO_2 catalyst.

and complex EPR signal appears after 5 min (II). The obtained EPR spectrum was divided into peaks and fitted by means of computer calculations (III) to give a triplet with an intensity ratio of 1:1:1, a sextuplet with an intensity ratio of 1:1:1:1:1:1, and a quadruplet with an intensity ratio of 1:2:2:1 (Fig. S6). For the quadruplet, values of α_N = 15 G and $\alpha_{\beta\text{-H}}$ = 15 G were determined, which correspond to DMPO-OH (α_N and $\alpha_{\beta\text{-H}}$ are the hyperfine coupling constants of the spins of the N and H atoms in DMPO-OH, respectively) [44,45]. In addition, for the sextuplet, values of α_N = 15.8 G and $\alpha_{\beta\text{-H}}$ = 19.1 G were determined, which correspond to the DMPO-CO_2^- anion, a C-centered carboxylic acid adduct (IV) [20,46–48]. Moreover, for the triplet, an α_N value of 16.6 G indicates the presence of DMPO-oxide. Thus, the signal corresponding to the DMPO-CO_2^- anion provides the most direct evidence that the CO_2 molecules present in the triboelectric plasma participate in a single-electron transfer process to form highly reactive CO_2^- species. The presence of DMPO-OH and DMPO-oxide were attributed to the generation of ·OH from water, and the oxidation of DMPO itself, respectively.

The reactive CO_2^- species adsorbed on the surface of the TiO_2 catalyst were then determined by in situ FT-IR difference spectroscopy, using the infrared spectrum of the TiO_2 catalyst before the reaction for comparison (Fig. 3b). In the presence of the triboelectric plasma, two infrared vibration absorption peaks are generated at 1677 and 1257 cm^{-1}, corresponding to the bending configuration of the CO_2 adsorbed on the TiO_2 surface [49,50]. This is consistent with the theoretical calculation results reported in the literature, wherein absorption peaks at 1689 and 1236 cm^{-1} were predicted for the CO_2 adsorbed on the oxygen vacancies of the anatase (101) plane. When the triboelectric plasma was turned off, these two peaks disappeared, thereby indicating that the triboelectric plasma can activate CO_2 to generate CO_2^- anions, which are adsorbed on the surface of the TiO_2 catalyst. The stretching vibration of bidentate carbonate (b-CO_3^{2-}) appeared at the region of about 1343 and 1545cm^{-1}, which is mainly due to the coordination between CO_2 molecule and Ti^{4+}-O^{2-} bond on the surface, through acid-base interaction [50].

3.3. Surface lattice oxygen activation by triboelectric plasma

In the CO_2 reduction process, the triboelectric plasma generates highly reactive CO_2^- species, and interacts with the surface of the TiO_2 catalyst. Hence, the surface changes of the TiO_2 catalyst were studied through a range of characterization and controlled experiments. More specifically, Fig. 4a illustrates the XPS results for the Ti 2p signals, wherein two absorption peaks can be seen at 458.7 and 464.4 eV, which correspond to the binding energies of $Ti2p_{3/2}$ and $Ti2p_{1/2}$, respectively (i.e., the Ti^{4+} state). Following the reaction, the proportion of Ti^{4+} ions in the sample remain constant, and two XPS splitting peaks at binding energies of 529.8 and 531.6 eV appear in the O 1s XPS spectrum (Fig. 4b and Table S1); these peaks were attributed to the surface lattice oxygen (O_{latt}) and oxygen vacancy (V_O) species, respectively. The proportion of $O_{latt}/(O_{latt} + V_O)$ on the surface of the fresh TiO_2 catalyst was 0.88, whereas the proportion of $V_O/(O_{latt} + V_O)$ was 0.12. Under Ar gas, the proportion of $O_{latt}/(O_{latt} + V_O)$ on the surface of the TiO_2 catalyst decreased to 0.84, and the proportion of $V_O/(O_{latt} + V_O)$ increased to 0.16. These observations indicate that under an Ar gas environment, the high-energy electrons and Ar^+ ions present in the triboelectric plasma can attack the O_{latt} species on the surface of the TiO_2 catalyst to break the Ti–O bonds and produce O atoms and V_O, as outlined below (Equation (5)):

$$O_{latt} \rightarrow O + V_O \tag{5}$$

Under a CO_2 gas environment, the proportion of $O_{latt}/(O_{latt} + V_O)$ on the surface of the TiO_2 catalyst was 0.87, and the proportion of $V_O/(O_{latt} + V_O)$ was 0.13, which are comparable to the values obtained for the fresh catalyst, thereby suggesting that the quantities of V_O and O_{latt} species are in dynamic equilibrium during the catalytic reaction. In a CO_2 atmosphere, under the bombardment of high-energy electrons, CO_2^- anions, and other particles, the surface Ti–O bonds are broken to produce O atoms and V_O. The O atoms can recombine with other O atoms present on the catalyst surface or in the gas phase to form O_2, as follows (Equation (6)):

$$O + O \rightarrow O_2(gas), \tag{6}$$

From the O 1s XPS results, it can be seen that the V_O concentration on the TiO_2 surface remains relatively constant, thereby suggesting that V_O consumption occurs in the reaction system in addition to the aforementioned V_O generation process. Based on our results and previous literature reports [8,9], it was considered that under a CO_2 gas environment, the reactive CO_2^- species adsorbed on the TiO_2 surface subsequently reacted with V_O to produce CO and O_{latt} as follows (Equation (7)):

$$CO_2^- + V_O \rightarrow CO + O_{latt} + e^- \tag{7}$$

This dynamic equilibrium of V_O on the catalyst surface was confirmed by EPR and PL investigations. More specifically, in the EPR spectrum of the TiO_2 catalyst (Fig. 4c), the signal at $g = 2.002$ corresponds to the electrons captured by V_O on the surface of the TiO_2 catalyst. Overall, the V_O concentration increased in the following order: TiO_2 samples under Ar < TiO_2 samples under CO_2 < fresh TiO_2 catalyst. Importantly, this trend was comparable to that observed for the concentration of the surface oxygen vacancies obtained by XPS. In addition, Fig. 4d illustrates the PL emission spectra of the TiO_2 samples recorded at different atmospheric conditions under an excitation wavelength of 300 nm. The emission peak at 525 nm was attributed to the electron recombination from the shallow donor below the conduction band (derived from the oxygen vacancies) to the holes in the acceptor valence band. Under both Ar and CO_2 conditions, the trend observed for the oxygen vacancies on the TiO_2 surface was consistent with those observed for the O 1s using XPS and EPR. Importantly, the dynamic balance of the oxygen vacancies on the surface of the TiO_2 catalyst ensures the sustainability of the triboelectric plasma catalytic reaction. As shown in Figs. S7–8, the activity and rate remained almost unchanged over six consecutive cycles, and the crystal structure and morphology of the catalyst remained stable.

3.4. Proposed mechanism for triboelectric plasma CO_2 reduction reaction

The mechanism and energy changes taking place during the CO_2 reduction reaction were investigated by theoretical calculations using anatase (101) as the model. Compared with the CO_2 molecules, the CO_2^- anion was stably adsorbed on the TiO_2 surface (Fig. 5a), forming a four-membered ring structure with an adsorption energy of − 0.31 eV (Fig. S9). The structure of the CO_2^- anion appeared to exhibit a degree of bending with a bond angle of 129.1°. The density of states (DOS) band diagram in Fig. 5b shows that a portion of the empty CO_2 energy level was filled relative to the non-adsorbed CO_2 molecules, and this energy level was reduced to the top of the valence band below the Fermi level. Although CO_2^- anion can be adsorbed on a clean TiO_2 surface, their dissociation barrier can reach up to 4.55 eV (Fig. S10), resulting in difficulties in direct decomposition. As a result, the CO_2^- anion migrates to the oxygen vacancies to form a more stable four-membered structure with an energy barrier of 0.40 eV (Fig. S11). Thus, the adsorption energy of the CO_2^- anion on the V_O sites of the TiO_2 surface was determined to be − 1.41 eV (Fig. S12); a new energy level was found to have formed in the DOS diagram (Fig. 5b), which resulted in a stronger binding energy between CO_2 and the TiO_2 surface. The aforementioned results indicate that compared with the clean TiO_2 surface, CO_2^- anion adsorbs more readily on the V_O sites of the TiO_2 catalyst. Following their adsorption, the CO_2^- anion can dissociate to produce CO, and the remaining O atoms can fill the V_O due to a low potential barrier of 0.18 eV. The desorption of the CO molecules from the TiO_2 surface can occur with an energy barrier of 0.29 eV. Finally, the surface of the TiO_2 catalyst is bombarded by the high-energy electrons, CO_2^- anions, and the other particles present in the triboelectric plasma, to produce V_O and O atoms. It has been reported in the literature that the formation energy of a V_O produced on the surface of TiO_2 is 1.2 eV [15]. Thus, in the triboelectric plasma-catalyzed CO_2 reduction reaction, the triboelectric plasma provides an energy resource for the generation of such species. The average electron energy of the triboelectric plasma over time was mapped at 50 μs (Fig. S13), and two reaction regions were identified, namely a cone with a radius of 0.15 mm and a wide cylinder with a diameter of 1.0 mm; the average energies of the electrons in these regions were determined to be 2.1–2.5 and 0.25–2.1 eV, respectively. In addition, in the energy-distribution curve of the central axis of the needle–plate (Fig. S14), the electrons present in the triboelectric plasma can be seen to possess sufficient energy to overcome the CO_2 activation process to form CO_2^- anions, to promote the dissociation of CO_2^- anions, and to generate V_O species.

Finally, to further illustrate the advantages of this catalytic system, the triboelectric plasma–semiconductor catalytic system was compared with common semiconductor catalytic systems, such as the photocatalytic system. More specifically, in the photocatalytic reaction system, the conduction band levels of almost all the semiconductors are much lower than those of the LUMO of CO_2. As a result, the transfer of the photogenerated electrons

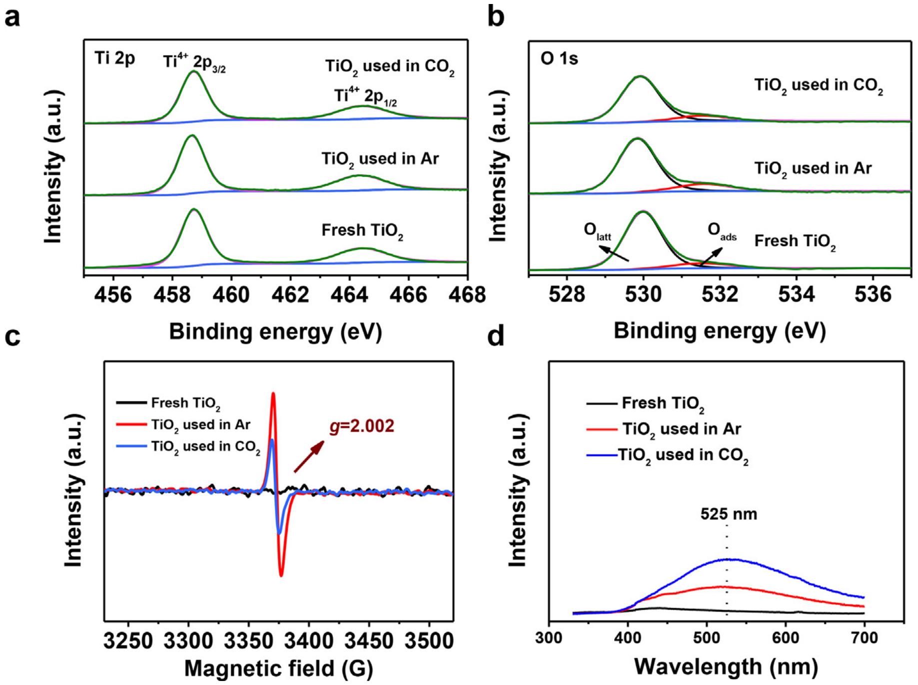

Fig. 4. Characterization of the TiO_2 catalyst. (a) Ti 3d and (b) O 1s X-ray photoelectron spectroscopy (XPS) results for the TiO_2 samples. (c) Electron paramagnetic resonance (EPR) spectra of the TiO_2 samples. (d) Photoluminescence (PL) spectra of the TiO_2 samples.

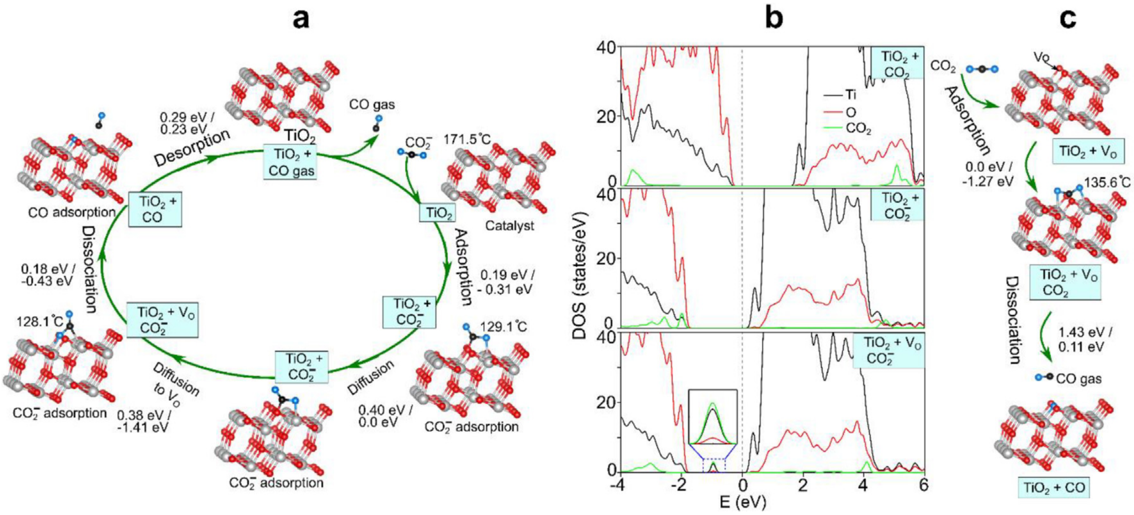

Fig. 5. Schematic of the energy and density of states (DOS). (a) Proposed reaction pathway for the triboelectric plasma catalytic CO_2 reduction process. The number in front of the oblique indicates the energy barrier, while the number behind the oblique represents the adsorption energy. (b) DOS under different conditions. The text in turquoise boxes indicates substrates adsorbed on the TiO_2 catalysts with/without oxygen vacancies. (c) Proposed reaction pathway for the photocatalytic CO_2 reduction reaction.

from the semiconductor photocatalyst to the CO_2 molecules and the formation of CO_2^- anions are challenging processes. This phenomenon was also confirmed by DFT calculations. In the photocatalytic reduction of CO_2, although the CO_2 molecules can be adsorbed on the V_O of the TiO_2 surface with an adsorption energy of – 1.27 eV, the decomposition barrier is high, i.e., 1.43 eV (Fig. 5c) [8,9,11]. Therefore, the activity of a standard TiO_2-based photocatalytic reaction system is extremely low at room temperature (25 °C) and pressure, and the energy efficiency is generally < 1 % [51,52]. Moreover, after the reaction, the V_O sites on the TiO_2 surface are blocked by strongly-bound oxygen atoms, thereby resulting in a reduced catalytic activity over time [53,54]. In contrast, in the triboelectric plasma–semiconductor catalytic system, a large number of low energy electrons originating from the triboelectric plasma are captured by CO_2, to form reactive CO_2^- anions, which effectively solves the mismatch issue between the semiconductor and CO_2 energy bands. Importantly, the decomposition barrier for the highly reactive CO_2^- anions present on the V_O is only 0.18 eV, which is 1.25 eV lower than that of the photocatalytic CO_2 reaction system. As a result, the former reaction can be performed at room temperature (25 °C) and pressure with an energy conversion efficiency of 5.3 % being achieved. Simultaneously, the reactive ions present in the triboelectric plasma can promote the regeneration of V_O and further improve the energy efficiency of the overall catalytic system.

4. Conclusion

We report a triboelectric plasma–metal oxide catalytic system for the reduction of CO_2 to CO at room temperature (25 °C) and atmospheric pressure. In this reaction system, TiO_2 exhibited an optimal activity of 0.14 $\text{mmol}\cdot g_{cat}^{-1}\cdot h^{-1}$, and the energy efficiency for the conversion of electrical to chemical energy was 5.3 %. The analyses using EPR and Fourier transform infrared spectroscopy indicated that a large number of slightly bent CO_2^- anions were produced in the triboelectric plasma, and that these anions adsorbed onto the surface of the TiO_2 catalyst. In addition, XPS, EPR, and photoluminescence experiments showed that the triboelectric plasma can activate the lattice oxygen species present on the surface of the TiO_2 catalyst to produce oxygen vacancies. Compared with CO_2 molecules, the CO_2^- anions adsorb more easily onto the TiO_2 surface, thereby facilitating the limiting CO_2 single-electron reduction step. Furthermore, the highly reactive species present in the triboelectric plasma can effectively promote the regeneration of oxygen vacancy sites. This study therefore provides a method for overcoming the energy bandgap limitations associated with the use of semiconductors in catalytic reactions. Currently, we are investigating the expansion of the triboelectric plasma–metal oxide catalytic system for the reduction of N_2, and our results will be presented in due course.

Data availability

Data will be made available on request.

Declaration of Competing Interest

The authors declare that they have no known competing financial interests or personal relationships that could have appeared to influence the work reported in this paper.

Acknowledgements

Funding from the National Natural Science Foundation of China (21902043, 61974040, 52202230) is also appreciated. We thank Dr. Xianwen Zhang at the State Key Laboratory of Catalysis, Dalian Institute of Chemical Physics, Chinese Academy of Sciences, for his help during the EPR experiments. We thank Prof. Jin Zhao at Hefei National Laboratory for Physical Sciences at the Microscale, University of Science and Technology of China, for her help during the DFT calculations.

Appendix A. Supplementary data

Supplementary data to this article can be found online at https://doi.org/10.1016/j.jcat.2023.01.031.

References

[1] S.N. Habisreutinger, L. Schmidt-Mende, J.K. Stolarczyk, Angew. Chem. Int. Ed. 52 (2013) 7372–7408.
[2] Y.K. Zhao, C.Y. Deng, D.J. Tang, L.Y. Ding, Y.C. Zhang, H. Sheng, H.W. Ji, W.J. Song, W.H. Ma, C.C. Chen, J.C. Zhao, Nat. Catal. 4 (2021) 684–691.
[3] I.V. Chernyshova, P. Somasundaran, S. Ponnurangam, Proc. Natl. Acad. Sci. USA 115 (2018) E9261–E9270.
[4] M.T. Tang, H.J. Peng, P.S. Lamoureux, M. Bajdich, F. Abild-Pedersen, Appl. Catal. B-Environ. 279 (2020).
[5] S. Kreft, D. Wei, H. Junge, M. Beller, EnergyChem 2 (2020).
[6] E. Gong, S. Ali, C.B. Hiragond, H.S. Kim, N.S. Powar, D. Kim, H. Kim, S.-I. In, Energy Environ. Sci. 15 (2022) 880–937.
[7] J.L. White, M.F. Baruch, J.E. Pander Iii, Y. Hu, I.C. Fortmeyer, J.E. Park, T. Zhang, K. Liao, J. Gu, Y. Yan, T.W. Shaw, E. Abelev, A.B. Bocarsly, Chem. Rev. 115 (2015) 12888–12935.
[8] J. Lee, D.C. Sorescu, X. Deng, J. Am. Chem. Soc. 133 (2011) 10066–10069.
[9] S.J. Tan, Y. Zhao, J. Zhao, Z. Wang, C.X. Ma, A.D. Zhao, B. Wang, Y. Luo, J.L. Yang, J.G. Hou, Phys. Rev. B 84 (2011).
[10] Y. Ji, Y. Luo, J. Am. Chem. Soc. 138 (2016) 15896–15902.
[11] W. Chu, Q. Zheng, O.V. Prezhdo, J. Zhao, J. Am. Chem. Soc. 142 (2020) 3214–3221.
[12] G. Chen, G.I.N. Waterhouse, R. Shi, J. Zhao, Z. Li, L.Z. Wu, C.H. Tung, T. Zhang, Angew. Chem. Int. Ed. 58 (2019) 17528–17551.
[13] J. Albero, Y. Peng, H. Garcia, ACS Catal. 10 (2020) 5734–5749.
[14] K. Li, B.S. Peng, T.Y. Peng, ACS Catal. 6 (2016) 7485–7527.
[15] P. Scheiber, M. Fidler, O. Dulub, M. Schmid, U. Diebold, W. Hou, U. Aschauer, A. Selloni, Phys. Rev. Lett. 109 (2012).
[16] G. Qing, R. Ghazfar, S.T. Jackowski, F. Habibzadeh, M.M. Ashtiani, C.P. Chen, M. R. Smith 3rd, T.W. Hamann, Chem. Rev. 120 (2020) 5437–5516.
[17] L. Hollevoet, F. Jardali, Y. Gorbanev, J. Creel, A. Bogaerts, J.A. Martens, Angew. Chem. Int. Ed. 59 (2020) 23825–23829.
[18] K.H.R. Rouwenhorst, F. Jardali, A. Bogaerts, L. Lefferts, Energy Environ. Sci. 14 (2021) 2520–2534.
[19] S.M. Li, B. Zhang, G.Q. Gu, D.Y. Fang, X.C. Xiang, W.H. Zhang, Y.F. Zhu, J. Wang, J. M. Cuo, P. Cui, G. Cheng, Z.L. Du, Adv. Sci. 9 (2022) e2201633.
[20] S.M. Li, B. Zhang, G.Q. Gu, X.C. Xiang, W.H. Zhang, X. Shi, K. Zhao, Y.F. Zhu, J.M. Guo, P. Cui, G. Cheng, Z.L. Du, Nano Energy 88 (2021).
[21] X. Shi, B. Zhang, L.L. Liu, Y.F. Zhu, X.C. Xiang, S.M. Li, K. Zhao, W.Y. Shang, G.Q. Gu, J.M. Guo, P. Cui, G. Cheng, Z.L. Du, ACS Appl. Nano Mater. 5 (2022) 1426–1434.
[22] X. Shi, S.M. Li, B. Zhang, J. Wang, X.C. Xiang, Y.F. Zhu, K. Zhao, W.Y. Shang, G.Q. Gu, J.M. Guo, P. Cui, G. Cheng, Z.L. Du, Nanomaterials 11 (2021) 3408.
[23] J. Cheng, W. Ding, Y. Zi, Y. Lu, L. Ji, F. Liu, C. Wu, Z.L. Wang, Nat. Commun. 9 (2018) 3733.
[24] A.J. Wu, J. Yang, B. Xu, X.Y. Wu, Y.H. Wang, X.J. Lv, Y.C. Ma, A.N. Xu, J.G. Zheng, Q.H. Tan, Y.Q. Peng, Z.F. Qi, H.F. Qi, J.F. Li, Y.L. Wang, J. Harding, X. Tu, A.Q. Wang, J.H. Yan, X.D. Li, Appl. Catal. B-Environ. 299 (2021).
[25] S. Kelly, A. Bogaerts, Joule 5 (2021) 3006–3030.
[26] L.R. Winter, J.G.G. Chen, Joule 5 (2021) 300–315.
[27] P. Mehta, P. Barboun, F.A. Herrera, J. Kim, P. Rumbach, D.B. Go, J.C. Hicks, W.F. Schneider, Nat. Catal. 1 (2018) 269–275.
[28] H. Ma, R.K. Sharma, S. Welzel, M.C.M. van de Sanden, M.N. Tsampas, W.F. Schneider, Nat. Commun. 13 (2022) 402.
[29] R. Snoeckx, A. Bogaerts, Chem. Soc. Rev. 46 (2017) 5805–5863.
[30] A. Bogaerts, E.C. Neyts, ACS Energy Lett. 3 (2018) 1013–1027.
[31] P. Mehta, P. Barboun, D.B. Go, J.C. Hicks, W.F. Schneider, ACS Energy Lett. 4 (2019) 1115–1133.
[32] G.X. Chen, V. Georgieva, T. Godfroid, R. Snyders, M.P. Delplancke-Ogletree, Appl. Catal. B-Environ. 190 (2016) 115–124.
[33] A.M. Vandenbroucke, M. Mora, C. Jimenez-Sanchidrian, F.J. Romero-Salguero, N. De Geyter, C. Leys, R. Morent, Appl. Catal. B-Environ. 156 (2014) 94–100.
[34] K. Zhang, A.P. Harvey, Chem. Eng. J. 405 (2021).
[35] S.R. Li, M. Ongis, G. Manzolini, F. Gallucci, Chem. Eng. J. 410 (2021).
[36] N. Lu, N. Liu, C.K. Zhang, Y. Su, K.F. Shang, N. Jiang, J. Li, Y. Wu, Chem. Eng. J. 417 (2021).
[37] G. Kresse, J. Hafner, Phys. Rev. B 48 (1993) 13115–13118.
[38] P.E. Blochl, Phys. Rev. B 50 (1994) 17953–17979.
[39] G. Kresse, J. Furthmiiller, Comput. Mater. Sci. 6 (1996) 15–50.
[40] J.P. Perdew, K. Burke, M. Ernzerhof, Phys. Rev. Lett. 77 (1996) 3865.
[41] S. Grimme, J. Antony, S. Ehrlich, H. Krieg, J. Chem. Phys. 132 (2010).
[42] G. Henkelman, B.P. Uberuaga, H. Jonsson, J. Chem. Phys. 113 (2000) 9901–9904.
[43] D. Schroder, C.A. Schalley, J.N. Harvey, H. Schwarz, Int. J. Mass Spectrom. 185–187 (1999) 25–35.
[44] B. Zhang, J. Li, Y.Y. Gao, R.F. Chong, Z.L. Wang, L. Guo, X.W. Zhang, C. Li, J. Catal. 345 (2017) 96–103.
[45] B. Zhang, J. Li, B.Q. Zhang, R.F. Chong, R.G. Li, B. Yuan, S.-M. Lu, C. Li, J. Catal. 332 (2015) 95–100.
[46] X.W. Liu, J.E. Zhong, L. Fang, L.L. Wang, M.M. Ye, Y. Shao, J. Li, T.Q. Zhang, Chem. Eng. J. 303 (2016) 56–63.
[47] L.L. Perissinotti, M.A. Brusa, M.A. Grela, Langmuir 17 (2001) 8422–8427.
[48] A. Molinari, L. Samiolo, R. Amadelli, Photochem. Photobiol. Sci. 14 (2015) 1039–1046.
[49] L.J. Liu, C.Y. Zhao, Y. Li, J. Phys. Chem. C 116 (2012) 7904–7912.
[50] K. Lorber, J. Zavašnik, I. Arčon, M. Huš, J. Teržan, B. Likozar, P. Djinović, ACS Appl. Mater. Interfaces 14 (2022) (1878) 31862–31863.
[51] J. He, C. Janaky, ACS Energy Lett. 5 (2020) 1996–2014.
[52] W. Shangguan, Q. Liu, Y. Wang, N. Sun, Y. Liu, R. Zhao, Y. Li, C. Wang, J. Zhao, Nat. Commun. 13 (2022) 3894.
[53] Y.A. Wu, I. McNulty, C. Liu, K.C. Lau, Q. Liu, A.P. Paulikas, C.J. Sun, Z.H. Cai, J.R. Guest, Y. Ren, V. Stamenkovic, L.A. Curtiss, Y.Z. Liu, T. Rajh, Nat. Energy 4 (2019) 957–968.
[54] X.D. Li, Y.F. Sun, J.Q. Xu, Y.J. Shao, J. Wu, X.L. Xu, Y. Pan, H.X. Ju, J.F. Zhu, Y. Xie, Nat. Energy 4 (2019) 690–699.